

Observation and Modeling of Geocoronal Charge Exchange X-Ray Emission During Solar Wind Gusts

M. Kornbleuth

Harvard-Smithsonian Center for Astrophysics, 60 Garden Street, Cambridge, MA 02138, USA

`mkornbleuth@cfa.harvard.edu`

ABSTRACT

Solar wind charge exchange (SWCX) X-rays are generated by the collision of highly charged solar wind ions and neutral gas. This phenomenon has been observed to take place around comets, in the heliosphere, and in the exosphere of Earth (geocorona). The X-rays emitted through heliospheric and geocoronal SWCX are significant contributors to the soft X-ray background seen in every observation. In order to study the geocoronal SWCX, twelve distinct solar wind gusts were studied which provided significantly increased solar wind flux and corresponding abrupt changes in geocoronal SWCX X-ray emission. Depending on the line of sight (LOS) of the X-ray telescope, these changes in X-ray emissions may be detected in the background of observations and can be extracted for study. Using the Community Coordinated Modeling Center's (CCMC) Block-Adaptive-Tree-Solarwind-Roe-Upwind-Scheme (BATS-R-US) model, the interaction of the chosen solar wind gusts with the Earth's magnetosphere is simulated to model the geocoronal X-ray emission during those gusts. The results from the simulations are compared with the changes in the X-ray background as measured by the *Chandra* X-ray Observatory.

Subject headings: solar wind — X-rays: diffuse background

1. Problem Statement

When highly charged solar wind ions interact with neutral gas, X-rays are emitted due to a process known as solar wind charge exchange (SWCX). This SWCX emission is prominent in both the heliosphere and also the Earth's outer atmosphere. For the heliosphere, SWCX occurs when the ions of the solar wind collide with the neutral H and He that has flowed into the solar system from the interstellar medium. For SWCX in the Earth's outer atmosphere, the solar wind interacts with the Earth's exosphere, or geocorona, and the neutral H atoms in the atmosphere exchange an electron with the solar wind ions.

With the advent of telescopes orbiting Earth, such as the *Chandra* X-ray Observa-

tory, the importance of understanding SWCX is becoming more evident. In the 1990's, the *ROSAT* All Sky Survey mapped the diffuse Soft X-ray Background (SXRb), which, at the time, was recognized to have three components: (1) absorbed extragalactic emission which followed a power law, (2) absorbed thermal emission from the Galactic halo ($\sim 2 \times 10^6$ K), and (3) unabsorbed thermal emission from the Local Bubble, which is a region surrounding the Sun and extending roughly 100 pc outward consisting of low density hot gas at approximately 10^6 K. While mapping the SXRb, *ROSAT* periodically experienced Long Term Enhancements (LTEs) in the detected X-ray event rate on the order of a few hours to a few days (Snowden et al 1995). In 1996, Lisse et al. observed X-ray emissions

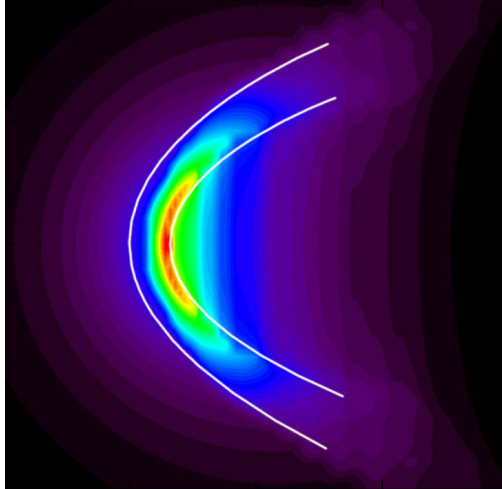
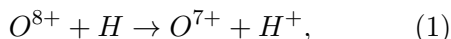


Fig. 1.—: Model geocoronal SWCX emission viewed perpendicular to the Sun-Earth axis (Robertson et al. 2006). Earth is at center and white curves show the bow shock and magnetopause. Emissivity, which is proportional to both ion and neutral density, is highest in the nose region because the solar wind comes closest to the Earth where neutral density is highest.

from comet Hyakutake. Cravens (1997) recognized that this was from SWCX, and it was soon realized that the same process caused the ROSAT LTEs (Cravens et al. 2001). Due to the nearness of geocoronal SWCX as opposed to heliospheric SWCX, the geocoronal SWCX can exhibit larger variations on short time scales because the SWCX of the exosphere is more abrupt, with less averaging over time and space, than SWCX in the heliosphere. During periods of time where there are no solar wind gusts, the heliospheric SWCX tends to dominate over the geocoronal SWCX and LTEs. Satellites in low-Earth orbit tend to be subjected to larger LTEs than satellites orbiting Earth at a greater distance because their lines of sight (LOS) often pass through longer and/or higher-emissivity paths through regions with SWCX emission.

An example of how charge exchange plays a role in X-ray contributions is given by



where in this case the O^{8+} ion, or the projectile, from the solar wind is interacting with the neutral hydrogen, or the target, of the exosphere. When the projectile and target col-

lide, the electric fields of the nuclei and electrons become superposed, leading to the distortion of energy levels. At certain distances, the energy levels of the projectile and target overlap to create “curve crossings” which enable the electron to transfer to the projectile at a higher energy level than its ground state. When the electron decays from this high energy level either from a radiative cascade or a decay directly to the ground state, it releases an X-ray photon (Wargelin et al. 2008).

In general, geocoronal SWCX can be found on the day side of Earth. Near the “nose” of the Earth’s magnetosphere, the solar wind encounters the Earth’s magnetic field and subsequently piles up, contributing a significant amount of geocoronal SWCX. Another location where geocoronal SWCX can be found is near the polar “cusps” since some ions interacting with the Earth’s magnetic field follow the lines which converge at the poles, leading to high ion densities. Because the neutral gas density is higher deeper in the Earth’s exosphere, the ability of the solar wind ions to penetrate relatively deep enhances the SWCX. In contrast, the SWCX is near-negligible in the magnetotail because the solar wind ions are excluded by the magnetic field in this re-

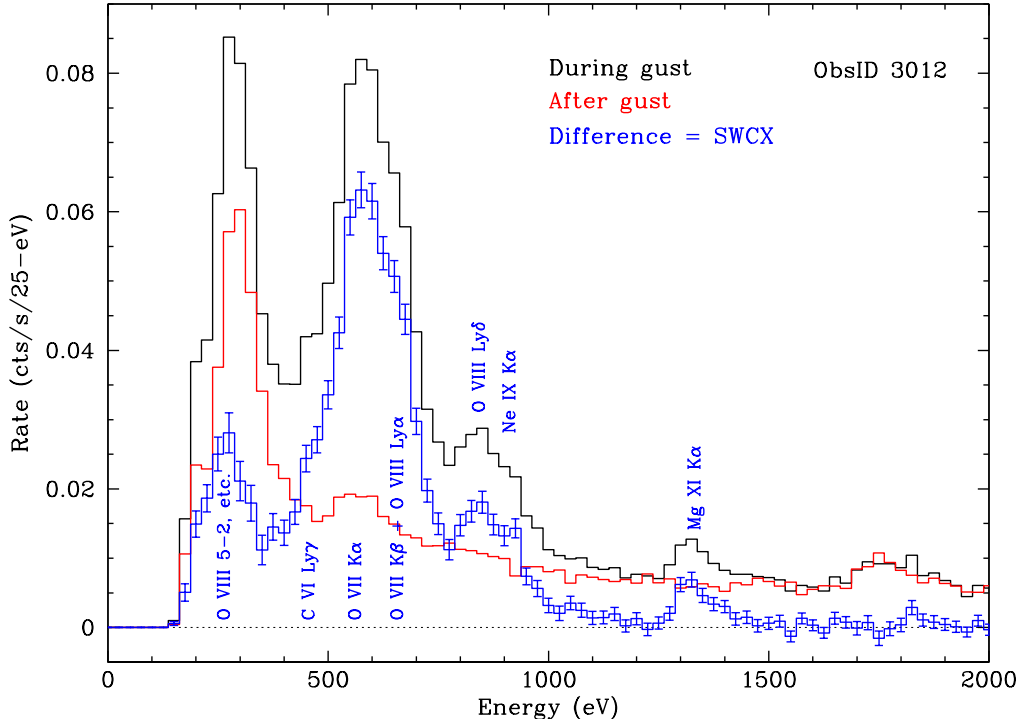


Fig. 2.—: Background X-ray spectrum of *Chandra* observation 3012 during a solar wind gust and after a solar wind gust. The difference between the two spectra represents the spectrum of the SWCX.

gion. During periods of solar wind gusts, the SWCX increases even more due to the increased ion densities interacting with the nose of the magnetosphere, which causes the compression of the magnetosphere and deeper penetration of the ions into the exosphere. This geocoronal SWCX emissivity is modeled in Figure 1, where it is seen how the emissivity is strongest along the nose because of increased penetration.

The purpose of this work is to examine the effect of solar wind gusts on the soft X-ray background. By utilizing the CCMC’s models and tools, the solar wind data can be compared with the X-ray background of *Chandra* observations to not only study the SWCX process, but also to examine the effect of SWCX on *Chandra* data. In particular, we focus on SWCX emission from O. Noting in Figure 2 an X-ray spectrum observed by *Chandra* during one of the selected gusts, the strong presence of O^{6+} $K\alpha$ and $K\beta$ and O^{7+} $Ly\alpha$ indicates the significant role O plays in geocoronal SWCX.

Using *Chandra* data from times during and after the gust, the data collected after the gust represents the non-SWCX X-ray background which can be subtracted from the data collected during the gust to find the spectrum of the SWCX. From these types of observations, it is determined that analysis of geocoronal SWCX takes place within the bounds of 500-700 eV in the X-ray spectrum.

This report is organized as follows: In section 2, I discuss the process used in the selection of gusts. In section 3, I give a description of the CCMC model that I used, along with a description of the CCMC tools I employed. In section 4, I present the results and findings of my work. In section 5, I discuss the uncertainties of my findings. In section 6, I present the conclusion.

2. Gust Selection

For the gusts selected, proton and O^{7+} fluxes can be calculated from ACE and *Wind*

TABLE 1
Chandra OBSERVATIONS AND INCIDENT SOLAR WIND FLUXES

ObsID	Starting Date	Exposure (ks)	CCDs	Max p Flux ($10^8 \text{ cm}^{-2}\text{s}^{-1}$)	Max O ⁷⁺ Flux ($10^4 \text{ cm}^{-2}\text{s}^{-1}$)
544	2000/03/22	10	I0123 S2	25.0	2.2
430	2000/10/13	39	I23 S123	14.5	67.9
2232	2001/02/19	129	I0123 S2	4.3	54.4
2255	2001/09/11	59	I0123 S3	15.8	60.6
2735	2002/09/29	65	I23 S23	13.4	92.4
3012	2002/12/19	43	I23 S123	24.1	90.7
3754	2003/07/25	128	I0123 S23	21.6	42.9
4215	2003/12/04	66	I0123 S2	7.3	84.9
4715	2004/12/05	6	I23 S123	33.2	9.4
6312	2005/06/23	40	I23 S123	30.3	9.2
5801	2005/10/24	44	I3 S123	17.6	60.6
6433	2006/09/23	70	I0123 S23	28.4	9.7

data using 1-hr binning for protons and 2-hr binning for O⁷⁺. Proton flux can be computed from SWEPAM data as

$$\Phi_p = n_p v_p \quad (2)$$

where v_p is the proton velocity of the solar wind. O⁷⁺ flux can be calculated from SWICS data as

$$\Phi_{O^{7+}} = n_{He} v_{He} \frac{n_O}{n_{He}} \frac{n_{O^{7+}}}{n_O} \quad (3)$$

where n_{He} and v_{He} are the helium ion density and velocity of the solar wind, n_O/n_{He} is the relative abundance of O and He, and $n_{O^{7+}}/n_O$ is the fraction of H-like Oxygen ions. Proton and O⁷⁺ fluxes, in addition to the general observational configurations of the *Chandra* observations may be noted in Table 1. For ObsIDs 2232, 2735, 3754, 4215 and 5801 *Wind* data is necessary to fill in gaps of *ACE* SWEPAM data. In addition, ObsIDs 2232, 2255 and 4215 require some proton density gaps to be filled in via proton density derived from *ACE* SWICS He density and an interpolated SWEPAM He/H ratio.

Comparing the peak ion flux values as provided in Table 1 to typical values shows a sig-

nificant difference. The typical proton density and solar wind speed at 1 AU in the ecliptic plane are 6.5 cm^{-3} and approximately 400 km^{-1} , respectively, leading to a flux of $2.6 \times 10^8 \text{ cm}^{-2}\text{s}^{-1}$. With a typical O/H abundance of 1/1780 and a 20% O⁷⁺ fraction, common for the slow solar wind (Schwadron & Cravens 2000), the resultant flux of O⁷⁺ is $2.9 \times 10^4 \text{ cm}^{-2}\text{s}^{-1}$. By comparison, the peak proton fluxes are about 13 times higher than normal and the peak O⁷⁺ fluxes are about 32 times higher than normal.

3. CCMC Models and Tools

For the purpose of modeling the interaction of selected solar wind gusts with the Earth's magnetosphere, the BATS-R-US model (version 20110131; Tóth et al. 2005, 2012) from the CCMC is utilized via the Runs on Request interface. The BATS-R-US code solves magnetohydrodynamic equations in three-dimensional space. The code employs an adaptive grid of rectangular blocks which vary in size in Geocentric Solar Magnetospheric coordinates. The X- axis points from the Earth to the Sun, while the XZ plane contains the Earth's magnetic dipole axis. Aside from time,

the BATS-R-US simulation requires inputs of proton density, velocity, temperature, and the magnetic field strength in its XYZ components. For the purpose of the simulation the Earth’s magnetic field is approximated by a dipole. As solar wind input data, the CCMC interface utilizes data from the *Advanced Composition Explorer (ACE)*, which provides observations from the Solar Wind Electron Proton Alpha Monitor (SWEPAM; McComas et al. 1998) and Solar Wind Ion Composition/Mass Spectrometers (SWICS/SWIMS; Gloeckler et al. 1998) instruments, as well as data from the *Wind* satellite’s Solar Wind Experiment (SWE; Ogilvie et al. 1995). As defaults, the CCMC uses *ACE* SWEPAM 64-sec proton data and 16-sec *ACE* Magnetic Field Experiment magnetic field data. As a backup for *ACE* data gaps, *Wind* 90-sec proton data may be used. In cases where neither the SWEPAM nor the *Wind* proton data is usable, proton densities are derived from 1-hr SWICS He density in conjunction with SWEPAM He/H data.

When creating the inputs for the BATS-R-US simulations, all SWEPAM and *Wind* proton data is gathered from the CCMC’s Input Files and Parameters Generation interface, where SWEPAM data can be called for a specific time in the appropriate CCMC format. For the proton data derived from SWICS He density, the 1-hr SWICS data is rebinned into 1-min bins to maintain consistency with the 1-min CCMC input data. In cases where the SWEPAM He/H data is good, the He/H ratio is utilized in conjunction with the He density to calculate the proton density. In situations where SWEPAM He/H data is flagged as bad, the He/H ratio is interpolated from adjoining data.

For the BATS-R-US simulations, time-of-flight adjustments are applied from the location of measured data to the leading edge of the simulation volume at 33 Earth radii (R_E) in front of Earth. Each simulation starts approximately one or two hours prior to the beginning of the *Chandra* observation in order to let the simulation “settle in.”

Chandra Observation IDs (ObsIDs) 430, 2232, 2255, 2735, 3012, 3754, 4215, and 5801 were selected because they occurred during times of peak O^{7+} flux (see Table 1), which, will, depending on the LOS, tend to yield peak SWCX. ObsIDs 544, 4715, 6312, and 6433 represent times of peak proton flux, when the higher proton flux compresses the magnetosphere, and the solar wind reaches higher density neutral H, thus increasing SWCX emissivity. Quantitatively, the magnetosphere size scales as $\Phi_p^{-1/6}$, where Φ_p is proton flux, and the neutral H density scales as $R^{-1/3}$ (Hodges 1994), where R is the distance from Earth. Neglecting variations in O abundance, the SWCX emissivity at the magnetopause is proportional to the solar wind flux and the density of neutral H, so higher proton flux contributes to a SWCX emissivity scaling of $\Phi_p^{3/2}$.

For the simulation grid, a high-resolution grid of 1,958,688 cells is employed. Auroral conductances that are driven by solar irradiance and electric currents which are aligned with the magnetic field are turned on. The Earth’s magnetic dipole is selected to update throughout the run. The simulation volume extends from -250 to +33 R_E along the X axis, and from -48 to +48 R_E along the Y and Z axes, with block sizes in the simulation ranging from 0.25 R_E near the Earth to 8 R_E at large distances. The simulation output is binned to 20 minute intervals with spatial blocking of 0.5 to 3 R_E .

To view the product of the simulation, I use the CCMC’s interface for the visualization of results of Earth’s environment and reduce the X-axis coverage to -50 to +25 R_E because geocoronal emissivity along *Chandra*’s LOS is generally negligible beyond this range. The specific outputs requested are proton density, velocity, temperature, and a status field that indicates whether the magnetic field in a particular simulation block is not connected to the Earth (status=0; in the solar wind), open and connect to either the south or north poles (status=1,2), or if the magnetic field line is closed (status=3; inside the magnetosphere). Figure

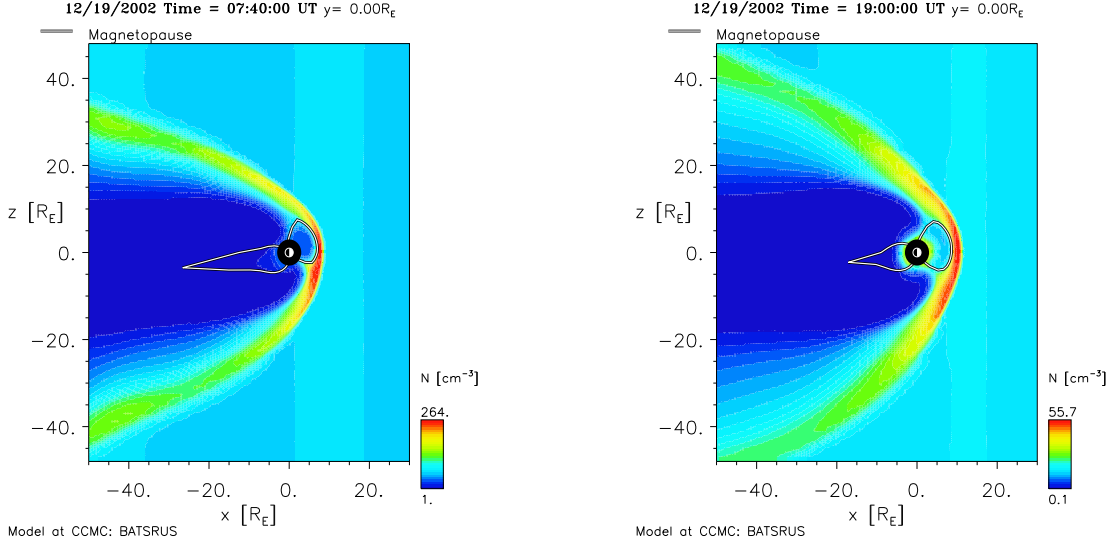


Fig. 3.—: The above plots are time slices of the solar wind density as generated by the CCMC’s interface for the visualization of results of Earth’s environment. (a) shows the interaction of the solar wind with the “nose” of the Earth’s magnetosphere (traced in white) during the solar wind gust and (b) shows the interaction following the gust.

3 shows two time slices of ObsID 3012 using the CCMC’s visualization interface, with Figure 3a showing a time slice during the solar wind gust and Figure 3b showing a slice following the gust. These slices demonstrate the effect of the gusts on the compression of the magnetosphere.

4. Results

Though the BATS-R-US simulation does not model minor ions, their densities can be calculated by making the assumption that relative ion abundances measured upwind are not significantly different from that which would be measured in the near-Earth environment. From this assumption, the density of a minor ion such as O^{7+} may be estimated as

$$n_{O^{7+}} = n_H \frac{n_{He}}{n_H} \frac{n_O}{n_{He}} \frac{n_{O^{7+}}}{n_O} \quad (4)$$

where n_H is taken from the BATS-R-US output, the He/H ratio is used from SWEPAM 1-hr data, and the remaining ratios are from SWICS ion data. Equation 4 can be applied to other minor ions such as C^{6+} , O^{8+} , and Ne^{9+} to calculate their densities.

The equation for calculating the brightness, B_{il} of a SWCX line l from ion i is

$$B_{il} = \frac{1}{4\pi} \int_0^\infty \epsilon_{il} dx \text{ phot cm}^{-2} \text{s}^{-1} \text{sr}^{-1} \quad (5)$$

where x is the distance from *Chandra* and the position-dependent emissivity is given by

$$\epsilon_{il} = v_c n_n n_i y_{il} \sigma_i \text{ phot cm}^{-3} \text{s}^{-1} \quad (6)$$

where v_c is the collision velocity, n_n is the density of the neutral H in the exosphere, n_i is the relevant ion density as may be derived from Equation 4, y_{il} is the net line emission yield per CX-excited ion, and σ_i is the total CX cross-section for the ion i . The cross-sections and line-yields are found in Wargelin et al. (2004) and its references. For n_n , the approximation from Cravens et al. (2001) of $n_H = 25(10R_E/r)^3 \text{ cm}^{-3}$ is used. The model results of the predicted SWCX emission light curves are plotted in Figure 4, along with the proton densities used as inputs for the BATS-R-US simulations and the integrated neutral H column density, N_H , along the LOS using

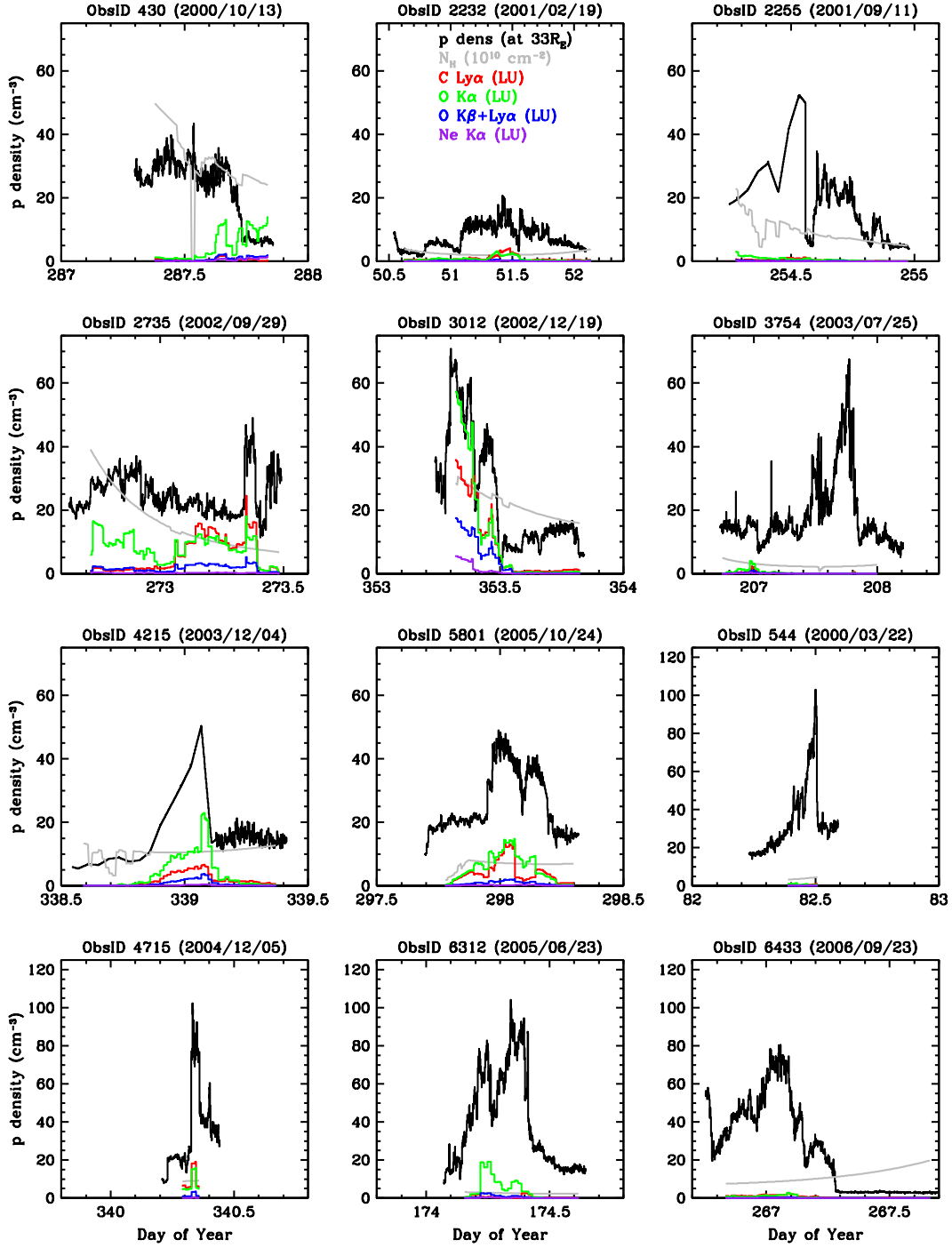


Fig. 4.—: Input proton density at $33R_E$ upwind of Earth and model results of five SWCX lines, as well as neutral H column density, N_H , along the LOS. SWCX lines use Line Units (LU) which are $\text{phot cm}^{-2} \text{s}^{-1} \text{ster}^{-1}$. Dips in N_H denote times when the LOS passes inside the magnetopause, where the solar wind ions cannot penetrate and there is no SWCX emission.

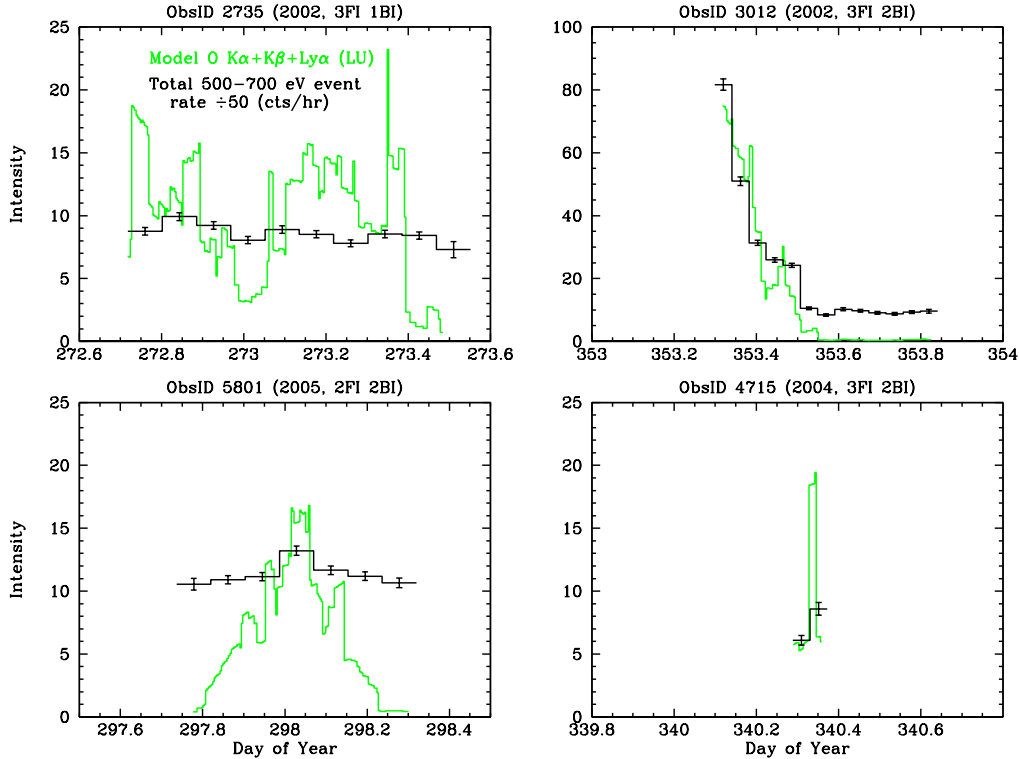


Fig. 5.—: Comparison of count rate and model brightness for O-lines. The 500-700 eV energy range includes the strongest SWCX lines (see Fig. 2). This range includes cosmic X-ray background as well as intrinsic detector background so the rate is never zero. Spectral fits will enable isolation of SWCX emission.

the program *geoCX.f* created by Dr. Brad Wargelin.

The results of comparing the count-rates of X-rays from the oxygen spectrum of *Chandra* background observations, derived using *Chandra* Interactive Analysis of Observations software package (CIAO)¹(Fruscione et al. 2006), to the model brightness as derived from BATS-R-US simulations for the case of four ObsIDs are presented in Figure 5. The figure demonstrates good correlation between X-ray emission and predicted SWCX brightness from model results; however, these plots represent rough results. In these plots, the *Chandra* results have not been adjusted for detector effi-

ciency. Initial limiting factors when comparing different *Chandra* observations from different years are which chips are used in the observation, since each chip has a different quantum efficiency (QE) for different energies, and a contaminant building up on the *Chandra* ACIS filter over time absorbs more low energy photons, which contributes to a decreasing QE. In addition, the units of measurement for the *Chandra* results are counts-in-energy-range which includes counts from the intrinsic detector background from cosmic rays, as well as the constant X-ray background from non-SWCX sources. Fully calibrated results will be derived from spectral fits over the next several weeks.

5. Discussion

There are several sources of uncertainty in this investigation. The first is that of the so-

¹*Chandra* data is prepared by removing point sources using the CIAO *wavdetect* tool. Times of increased particle-induced background are removed via the CIAO *deflare* tool. The background spectrum is scaled to energies where there is no SWCX in order to subtract particle background.

lar wind data, where, for example, there is an uncertainty in the SWICS ion densities of approximately $\pm 30\%$. This solar wind uncertainty carries over to the BATS-R-US simulation because of its foundation on observed data. In addition, the boundary between the solar wind and magnetopause is not exact and there is a potential factor of ± 2 uncertainty in the neutral H density. Regarding components of the position-dependent emissivity, σ_i and y_{il} combine for an approximate uncertainty of $\pm 30\%$.

The heliospheric SWCX will also vary with time producing another source of uncertainty. This factor is less significant, though, because it is less closely correlated with the local solar wind due to the relevant emission volume of the heliospheric SWCX being several AU. For a LOS with constant X (i.e. tangent to the solar wind “wavefront”), as in the cases of ObsIDs 2735 and 4715, the temporal correlation will be tighter than usual. Though this is not being modeled, qualitative statements and rough estimates can be made.

Regarding other potential sources of error, interpolated proton densities used in the BATS-R-US simulations from 1-hr SWICS Helium and 1-hr SWEPAM He/H data may contribute to a decrease in the correlation between periods of high solar wind flux and X-ray emission in the geocorona. Since this interpolated data is derived from 1-hr data and the input for BATS-R-US is submitted at 1-min intervals, the linear nature of the interpolation creates a degree of uncertainty of extended time scales; however, this is only applicable to a small sampling of the observed and modeled data. In general, the 1-hr interpolated data is only used at the beginning of observations, and is restricted to ObsIDs 2232, 2255 and 4215.

6. Conclusion

Through the use of BATS-R-US modeling and *Chandra* observations, a correlation is observed between solar wind gusts and X-ray emission for at least some observations. Proper spectral fits to obtain line brightness

for direct comparison with our model will tell us more. In several cases, changes in the SWCX will be too small to measure. While this project is not yet completed, the model results and observations do indicate geocoronal SWCX emission despite the weakness of the X-ray emissions. This emission takes place within a few tens of Earth radii of the planet, and mainly consists of the interaction of minor solar wind ions such as O^{7+} and the neutral H of the exosphere.

MK would like to acknowledge the support of Dr. Brad Wargelin, who supervised, directed and reviewed the work, while pointing out problems and asking for additional investigations. Dr. Wargelin also wrote *geoCX.f* program, which integrates emissivity along the LOS, and made some plots of the results. MK did the remainder of the work presented in this report. MK is supported by the Smithsonian Institution’s Competitive Grants Program for Science contract 40488100HH0045 3D.

REFERENCES

- Cravens, T. E. 1997, *Geophys. Res. Lett.*, 24, 105
- Cravens, T. E., Robertson, I. P., & Snowden, S. L. 2001, *J. Geophys. Res.*, 106, 24883
- Fruscione, A., et al. 2006, *Proc. SPIE*, 6270, 62701V
- Gloeckler, G. J. et al. 1998, *Space Sci. Rev.*, 86, 497
- Hodges, R. R., Jr. 1994, *J. Geophys. Res.*, 99, 23229
- Lisse, C. M., et al. 1996, *Science*, 274, 205
- McComas, D. J., Bame, S. J., Barker, P., Feldman, W. C., Phillips, J. L., Riley, P., & Griffee, J. W. 1998, *Space Sci. Rev.*, 86, 563
- Ogilvie, K. W., et al. 1995, *Space Sci. Rev.*, 71, 55
- Robertson, I. P., Collier, M. R., Cravens, T.E., & Folk, M. C. 2006, *J. Geophys. Res.*, 111, A12105
- Schwadron, N. A., & Cravens, T. E. 2000, *ApJ*, 544, 558
- Snowden, S. L., et al. 1995, *ApJ*, 454, 643

- Tóth, G., et al. 2012, Journal of Computational Physics, 231, 870
- Tóth, G., et al. 2005, Journal of Geophysical Research (Space Physics), 110, 12226
- Wargelin, B. J., Beiersdorfer, P., Brown, & G. V. 2008, Can. J. Phys., 86, 151
- Wargelin, B. J., Markevitch, M., Juda, M., Kharchenko, V., Edgar, R., & Dalgarno, A. 2004, ApJ, 607, 596